Composition-controlled ternary Rh–Pd–Pt solid-solution alloy nanoparticles by laser irradiation of mixed solution of metallic ions

Md Samiul Islam Sarker[a)]
Institute of Multidisciplinary Research for Advanced Materials (IMRAM), Tohoku University, Aoba-ku, Sendai 980-8577, Japan; and Department of Physics, University of Rajshahi, Rajshahi 6205, Bangladesh

Takahiro Nakamura and Shunichi Sato
Institute of Multidisciplinary Research for Advanced Materials (IMRAM), Tohoku University, Aoba-ku, Sendai 980-8577, Japan

(Received 6 November 2013; accepted 4 March 2014)

We present a bottom-up fabrication route to fabricate solid-solution Rh–Pd–Pt ternary alloy nanoparticles (NPs), with well-controlled compositions through femtosecond laser irradiation of a mixed solution of metallic ions, without any reducing agents and complicated processes. The structure of fabricated NPs was crystalline, and formation of solid-solution alloy formation was confirmed by electron and x-ray diffraction measurements. The crystalline nature of alloy NPs was also confirmed through high-resolution transmission electron microscope measurement. According to energy dispersive spectroscopy analysis, elemental composition of an individual NP was almost the same as the initial feeding ratio of ions in the mixed solutions. The electronic state of the element in alloy NPs was confirmed to be pure metal by XPS measurement. The structural studies of Rh–Pd–Pt NPs suggested that the demonstrated technique opens up a new dimension for the fabrication of NPs, which has well-controlled properties for practical use in various fields.

I. INTRODUCTION

The preparation of alloy NPs with controlled size and composition is of special importance, particularly in catalytic and optical applications.[1,2] For example, the binary and ternary alloy NPs exhibit excellent catalytic activity, such as hydrogenation,[3] CO oxidation,[4] and glucose oxidation.[5] Among the large number of possible elemental combinations, pure rhodium (Rh), palladium (Pd), and platinum (Pt) as well as their binary and ternary alloy NPs with controlled composition, size, and shape are of special interest as three-way catalysts for automobile emission control.[6] For example, enhanced catalytic activity of Rh–Pd alloy NPs was found in CO oxidation by O_2 compared with those of pure Rh and Pd.[7] Moreover, enhanced catalytic activity for NO_x reduction, CO chemisorption, and hydrogenation was investigated for Rh–Pt alloy NPs.[8,9] Though there is a possibility of prominent catalytic property for the ternary NPs, only very few research studies have been reported the formation of ternary alloy NPs to date. It has been reported that Pt–Ru–Co ternary NPs fabricated through an emulsion technique showed higher catalytic activity than Pt–Ru binary NPs toward methanol oxidation.[10] The ternary Au@Pd@Pt core–shell NPs from polyvinylpyrrolidone-based aqueous solution demonstrated higher catalytic activity than Au@Pt binary core–shell or pure Pt NPs.[11] The Au–Ag–Pt ternary NPs showed several times higher catalytic activity for aerobic glucose oxidation than pure Au NPs.[12] The hydrogenation of olefin was also studied through core–shell Pd@Ag@Rh NPs,[13] and showed higher catalytic activity than its pure metal NPs or binary alloy NPs. Alloy-like Au–Ag–Pd NPs were fabricated by Nd:YAG pulsed laser irradiation of a mixture of Au, Ag, and Pd colloids[14] showing efficient catalytic activity for Heck coupling reaction. In the experiment, these NPs were produced through melting and evaporation of mixed metal colloids using laser irradiation as a thermal source. The superior performance of ternary NPs compared to pure or binary system is the strong motivation toward the synthesis of fascinating ternary alloy NPs.

In general, production of solid-solution ternary Rh–Pd–Pt alloys in bulk is very difficult, because Rh–Pd, Rh–Pt, and Pd–Pt systems have large miscibility gaps in their binary phase diagrams. Normally, these gaps arise from different electronic energy levels of Rh, Pd, and Pt. On the contrary, it is reported that electronic structures of these elements in a nanometer-sized particle retain, and therefore nanometer-sized particles have a favor to form homogeneous alloys and no rehybridization occurs due to band formation.[15]

We have demonstrated binary Au–Ag, Au–Pt, Rh–Pd, and Rh–Pt, and ternary Au–Ag–Pt[16–19] NPs formation with fully tunable compositions by femtosecond laser irradiation of mixed ion solutions. In the case of tightly focused femtosecond laser irradiation in a solution, nonlinear

[a)]Address all correspondence to this author.
e-mail: samiul@mail.tagen.tohoku.ac.jp
DOI: 10.1557/jmr.2014.62

 © Materials Research Society 2014

https://doi.org/10.1557/jmr.2014.62 Published online by Cambridge University Press

optical processes such as multiphoton absorption and avalanche ionization can take place due to high photon density of strongly focused beam in a condensed matter. Therefore, interaction of laser pulses with neat water molecules produces reactive species.[20] Among them, solvated electrons and hydrogen radicals will act as reducing agents for metallic ions; as a result, metal or alloy NPs are formed.

Based on our successful preparation of binary Rh–Pd and Rh–Pt alloy NPs,[18] we extended our approach toward the synthesis of ternary Rh–Pd–Pt alloy NPs in this study. The morphology, crystal structure, elemental composition, and electronic state of fabricated NPs were evaluated by means of TEM, XRD, EDS, and XPS.

II. MATERIALS AND METHODS

A. Preparation of mixed solutions

Rhodium (III) chloride trihydrate ($RhCl_3{\cdot}3H_2O$, 99.5%) was obtained from Wako pure chemical industries Ltd. (Osaka, Japan). Palladium (II) chloride ($PdCl_2$, 99.9%) and hydrogen hexachloroplatinate (IV) hexahydrate ($H_2PtCl_6{\cdot}6H_2O$, 99.9%) were purchased from Sigma Aldrich Co. (St. Louis, MO). All chemicals were used without further purification. Initially, Rh, Pd, and Pt aqueous solutions were prepared by dissolving $RhCl_3{\cdot}3H_2O$, $PdCl_2$, and $H_2PtCl_6{\cdot}6H_2O$ powder in ultra pure water separately with a concentration of 2.5×10^{-4} M and then mixed with different molar ratios of 33:33:33, 50:25:25, 25:50:25, and 25:25:50. Samples were denoted by the molar fraction of Rh, Pd, and Pt ions in the solutions. For example, Rh33Pd33Pt33 denotes the solution containing 33% Rh, 33% Pd, and 33% Pt ions. All the solutions were transparent and no differences were observed. Figure 1(a) shows the UV-visible absorption spectra of solutions prepared with different molar fractions of Rh, Pd, and Pt ions using a UV-visible spectrometer (Jasco Co., Tokyo, Japan, V630 iRM). It is observed that the absorption spectra of the solutions were similar and showed strong peaks in UV region originated from the absorption of ions.

B. Laser irradiation condition

A quartz cuvette having a 3 mL solution was used as a target. Laser irradiation was performed by using a Ti:Sapphire laser (Spitfire Pro, Spectra-physics Co. Santa Clara, CA), which generates femtosecond laser pulses (wavelength: 800 nm; pulse width: 100 fs; average pulse energy: 5.8 mJ; repetition rate: 100 Hz). The beam was focused by an aspheric lens with the focal length of 8 mm and the numerical aperture of 0.5. The beam diameter was estimated to be 175 μm by taking into account of spherical aberration of refractive index mismatch of the cuvette and the solution. The beam intensity was 2.2×10^{14} W/cm^2 at the focal spot, which assumed no loss in the sample solution and the optics that are used in the experiment. Irradiation time was set to 30 min for all samples.

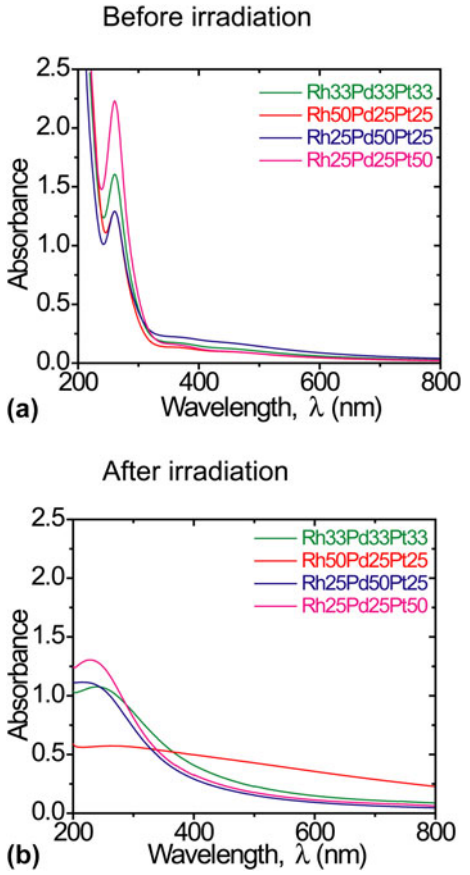


FIG. 1. UV-visible absorption spectra of mixed solutions for different fractions of Rh, Pd, and Pt ions (a) before and (b) after irradiation.

C. Characterization

The optical absorption properties of metal colloids were characterized by UV-visible absorption spectra ranging from 200 to 800 nm using the cuvette which is used for laser irradiation. The size, shape, and corresponding selected-area electron diffraction (SAED) patterns of fabricated NPs were obtained by a transmission electron microscope (TEM; JEOL, JEM2000EXII, JEOL Ltd., Tokyo, Japan) that was operated at an acceleration voltage of 200 kV. TEM samples were prepared by placing a few drops of irradiated colloids onto a carbon-coated copper microgrid (Microgrid type B, Okenshoji Co., Ltd., Tokyo, Japan) and dried in vacuo at room temperature. The averaged size and size distribution of particles were determined by analyzing the particles using a particle counting software (imageJ 1.46d), which was produced by National Institutes of Health (NIH). The zeta potential was measured to check the stability of a colloidal solution using nanoparticle analyzer (SZ-100, Horiba Ltd, Kyoto). High-resolution TEM images were taken to determine the crystal structure of NPs with a FEI-TITAN X-FEG TEM in STEM mode (Hillsboro, OR) operated at 300 kV. Energy dispersive x-ray spectrum [Energy dispersive x-ray

https://doi.org/10.1557/jmr.2014.62 Published online by Cambridge University Press

spectroscopy (EDS), Noran, Napoli, Italy, Voyager III light element EDS system] analysis of the specimen was performed to measure the elemental composition of NPs. The crystalline structures of NPs were determined by powder x-ray diffraction (XRD, RINT-V, Rigaku Co., Tokyo, Japan). A computerized diffractometer equipped with a Ni-filtered Cu K_α (λ = 0.15406 nm) x-ray source and a goniometer with a solid state Ge detector was used to obtain XRD profiles by $\theta-2\theta$ scan. The as-prepared sample was collected using a freeze drier, and then it was placed onto a single crystal silicon substrate with no diffraction peaks in the scan range and subjected it for XRD measurement. X-ray photoelectron spectroscopy (XPS) was used to analyze the electronic states of NPs (Shimadzu/KRATOS, Kyoto, Japan, with Al K_α radiation; AXIS-165). The spectrometer was equipped with a concentric hemispherical analyzer (CHA), which used 8 channeltron detectors. During inspection, the base pressure of the chamber was 10^{-9} Torr. The pass energy was 80 eV during the survey scan and 20 eV for the window scan.

III. RESULTS AND DISCUSSION

During laser irradiation, generation of tiny bubbles was observed near the focal point. Bubbles were identified as oxygen and hydrogen by the chromatographic analysis (Shimadzu Co., Kyoto, GC-8A). The formation of bubbles seemed to be due to the decomposition of water molecules through laser induced optical breakdown.[21] The solutions were initially clear and transparent but gradually changed to dark brown during laser irradiation. It is noted that the color change had no significant effect on the particle synthesis because the solutions were almost

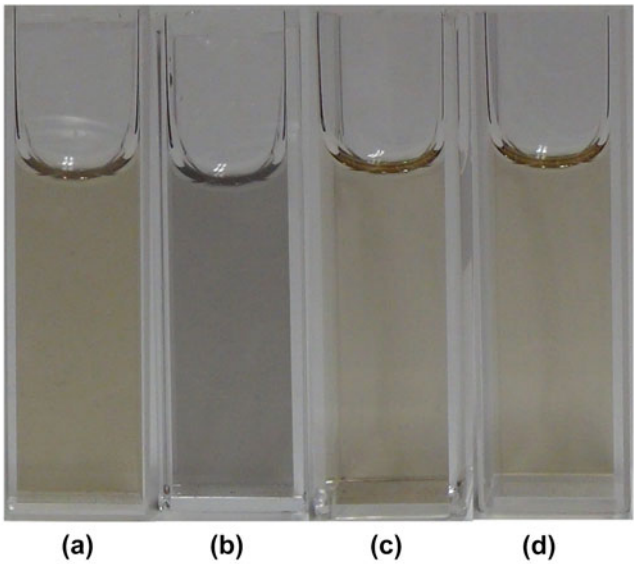


FIG. 2. Mixed solution of Rh, Pd, and Pt ions with different molar fractions after irradiation (a) Rh33Pd33Pt33, (b) Rh50Pd25Pt25, (c) Rh25Pd50Pt25, and (d) Rh25Pd25Pt50.

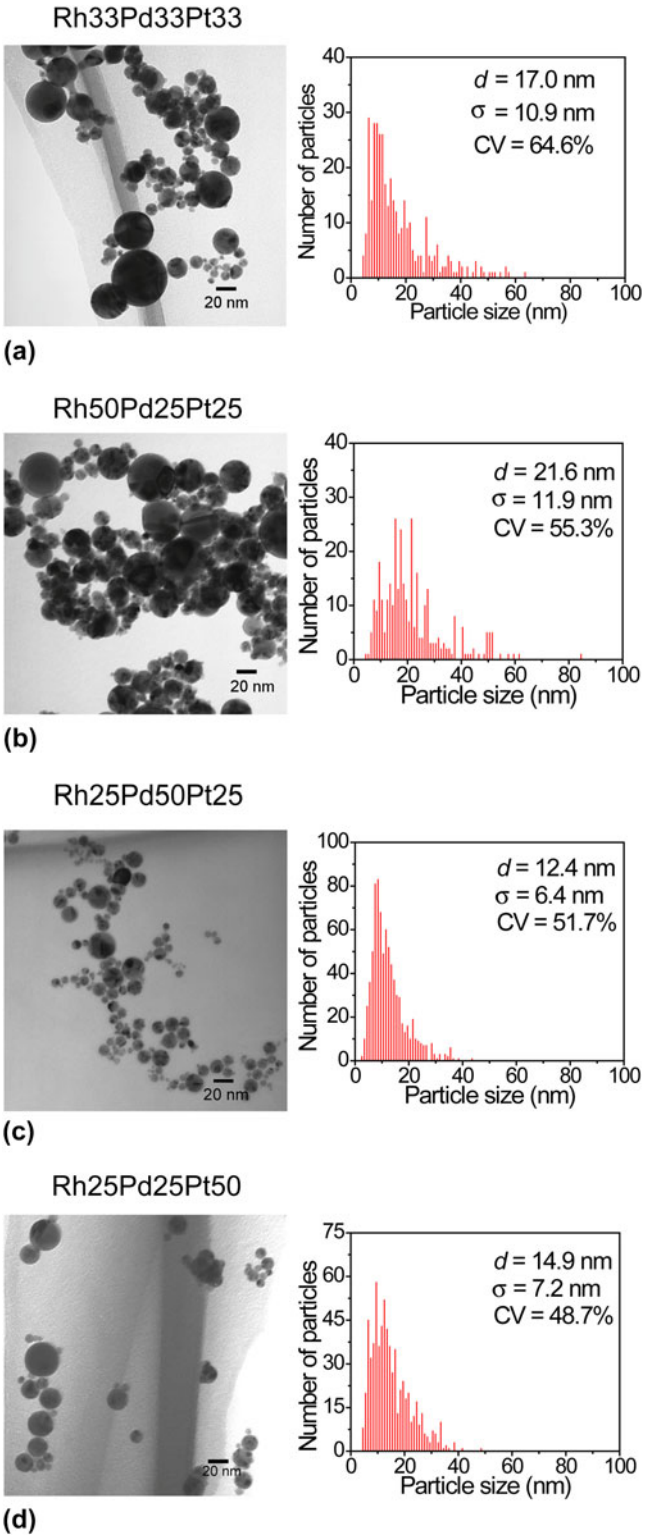


FIG. 3. TEM images and corresponding size distributions of as-prepared NPs in (a) Rh33Pd33Pt33, (b) Rh50Pd25Pt25, (c) Rh25Pd50Pt25, and (d) Rh25Pd25Pt50 solutions. Mean particle size (*d*), standard deviation (*s*), and coefficient of variation (CV) are shown in the inset.

https://doi.org/10.1557/jmr.2014.62 Published online by Cambridge University Press

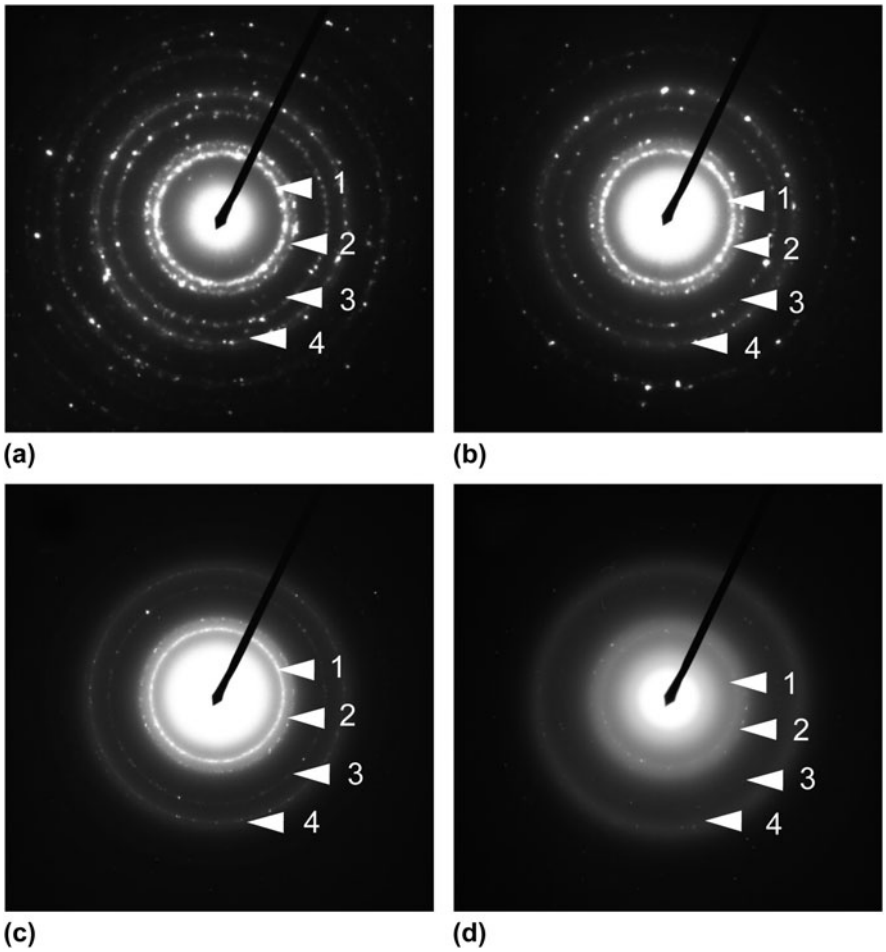


FIG. 4. Typical SAED pattern of NPs fabricated in the mixed solutions of (a) Rh33Pd33Pt33, (b) Rh50Pd25Pt25, (c) Rh25Pd50Pt25, and (d) Rh25Pd25Pt50. Diffraction rings correspond to the lattice planes of (111), (200), (220), and (311) for fcc crystalline.

transparent at the laser wavelength (800 nm) even after the laser irradiation as shown in Fig. 1(b). The color of the solution after irradiation depends on the molar ratios of Rh, Pd, and Pt ions as shown in Fig. 2. Figure 1(b) depicts the UV-visible absorption spectra of solutions for different mixing ratios of Rh, Pd, and Pt ions after irradiation. As shown in Fig. 1(a), all mixtures exhibit strong absorption peak at 261 nm due to the presence of $[PtCl_6]^{2-}$ ion corresponding metal–ligand (M–L) charge transfer. Interestingly, the formation of metal NPs is indirectly suggested from the fact that absorption peaks due to the $[PtCl_6]^{2-}$ ion disappeared after laser irradiation [Fig. 1(b)].

TEM analysis has been performed to investigate average size, morphology, and crystalline structure of the fabricated NPs. Figure 3 shows a representative set of bright-field TEM images of as-produced NPs in Rh–Pd–Pt mixed solutions with different molar fractions of Rh, Pd, and Pt ions. The size distribution of NPs is shown on the right-hand side of each TEM image. The size of the dispersed NPs was obtained by image processing software (imageJ) from at least three areas randomly chosen from each TEM image. The average sizes with its standard deviation of Rh–Pd–Pt system are 16.9 ± 10.9, 21.6 ± 11.9, 12.4 ± 6.4, and 14.9 ± 7.2 nm for Rh33Pd33Pt33, Rh50Pd25Pt25, Rh25Pd50Pt25, and Rh25Pd25Pt50, respectively. The shape of the NPs was almost spherical but the size distribution was relatively broad (coefficient of variation, CV ≈ 50%).

TABLE I. Interplanar spacings for Rh–Pd–Pt alloy NPs obtained from SAED patterns.

	d (Å)			
Sample	111	200	220	311
Rh33Pd33Pt33	2.235	1.936	1.369	1.167
Rh50Pd25Pt25	2.224	1.926	1.361	1.162
Rh25Pd50Pt25	2.234	1.934	1.365	1.163
Rh25Pd25Pt50	2.240	1.940	1.371	1.166

In the case of Rh–Pd–Pt system, it is noticeable that the average size of particles was fluctuated with the ratio of metal ions in the solution; the maximum average particle size was observed for the Rh50Pd25Pt25 case, and the average size decreased with decreasing Rh content. Similar

https://doi.org/10.1557/jmr.2014.62 Published online by Cambridge University Press

tendency has been confirmed for the bimetallic case.[18] Although further investigation should be required, this may due to the differences of surface energy, interatomic distance, and atomic radius of Rh, Pd, and Pt played an important role in the reaction resulting in the different size of the prepared NPs.[22]

The colloidal solutions remained dispersed for several days after irradiation depending on the fraction of Rh ions in the solution without any dispersants. The temporal stability of NPs can be explained from ζ potential measurement. The ζ potential of Rh33Pd33Pt33, Rh50Pd25Pt25, Rh25Pd50Pt25, and Rh25Pd25Pt50 colloidal solutions after irradiation were −28.5, −17.8, −27.5, and −29.8 mV, respectively. It could be seen that the ζ potential of Rh50Pd25Pt25 colloidal solution was smaller, compared with those of other three colloidal solutions and started to precipitate within a day, and this is due to the less stability of the colloid having a large fraction of Rh ions. Although further investigation should be needed for the less stability of the colloidal solution with higher rhodium content, temporary stability may be achievable due to electrostatic repulsion between particles formed in the high intensity laser irradiation reaction.

To assess the ternary alloy NPs formation, the interplanar spacing of NPs was obtained by SAED pattern and compared with that from Vegard's law. The interplanar spacing (d_{hkl}) of a given lattice plane (hkl) was estimated using the formula as follows;

$$r \cdot d_{hkl} = L \cdot \lambda \quad , \tag{1}$$

where r is the ring radius of the SAED pattern, L is the camera length after calibration by the standard sample (L = 82.40 cm), and λ is the wavelength of the electron beam (λ = 0.002507 nm). Figure 4 shows a representative set of SAED patterns of NPs fabricated in the solutions with different mixing ratios of Rh, Pd, and Pt ions. The SAED patterns exhibit four major-ring characteristics of face-centered cubic (fcc) structure having (111), (200), (220), and (311) planes. The estimated interplanar spacings of NPs fabricated in the mixed solution corresponding to different planes are summarized in Table I.

To compare the experimental data, the theoretical interplanar spacings were also summarized in Table II that were estimated for a given hkl planes of Rh–Pd–Pt ternary alloys with different compositions of the elements by considering a linear-weighted composition for those of pure elements by Vegard's law[23];

$$d_{hkl} = x_1 \cdot d_{hkl,\mathrm{Rh}} + x_2 \cdot d_{hkl,\mathrm{Pd}} + (1 - x_1 - x_2) \cdot d_{hkl,\ \mathrm{Pt}} \quad , \tag{2}$$

where $d_{hkl,\mathrm{Rh}}$, $d_{hkl,\mathrm{Pd}}$, $d_{hkl,\mathrm{Pt}}$ are the interplanar spacings of Rh, Pd, and Pt from Joint Committee for Powder Diffraction Standards (JCPDS) card No. 05-0685, 46-1043, and 040802 for Rh, Pd, and Pt, respectively, and x_1 and x_2 are the molar fractions of Rh and Pd in the precursor solutions, respectively.

It is clearly observed that the interplanar spacings obtained from SAED patterns (Table I) are agreed well with those estimated by Vegard's law (Table II).

For more detailed structural analysis of fabricated NPs, XRD measurements were performed for all the samples. Figure 5(a) shows a set of XRD patterns of NPs prepared in the solutions with different mixing ratios of Rh, Pd, and Pt ions. The typical XRD peaks of NPs exhibited the characteristics of fcc structure. The diffraction peak from (111) plane of every sample presented in Fig. 5(b) was a single peak indicating that no phase segregation occurred.

TABLE II. Theoretical interplanar spacings for Rh–Pd–Pt alloy obtained by Vegard's law.

	d (Å)			
Materials	111	200	220	311
Rh33Pd33Pt33	2.236	1.936	1.369	1.167
Rh50Pd25Pt25	2.226	1.927	1.363	1.162
Rh25Pd50Pt25	2.238	1.938	1.370	1.168
Rh25Pd25Pt50	2.243	1.942	1.373	1.171

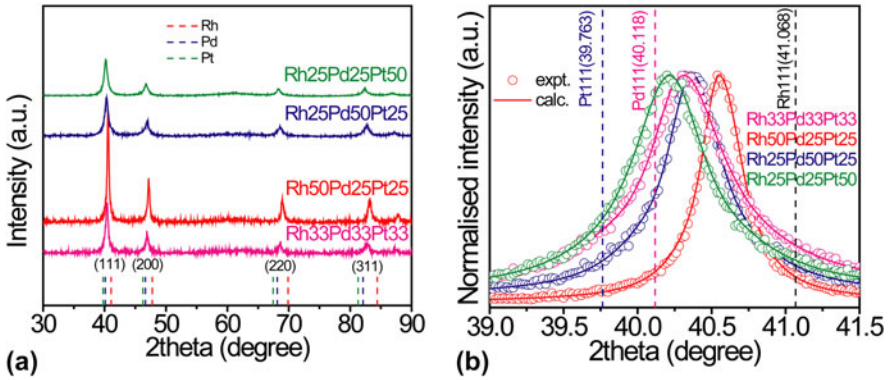


FIG. 5. (a) XRD patterns of NPs in the mixed solutions of Rh, Pd, and Pt ions and (b) diffraction peaks of NPs from (111) planes of the samples.

https://doi.org/10.1557/jmr.2014.62 Published online by Cambridge University Press

TABLE III. Lattice parameters [a (Å)] for Rh–Pd–Pt alloy NPs calculated from the XRD peaks of (111) plane.

Sample	2θ (°)	d (Å)	I (cps)	FWHM (°)	a (Å)	Size_{XRD} (Å)
Rh33Pd33Pt33	40.330	2.234	97	0.437	3.870	202.2
Rh50Pd25Pt25	40.530	2.224	222	0.285	3.852	310.6
Rh25Pd50Pt25	40.267	2.237	74	0.632	3.876	139.8
Rh25Pd25Pt50	40.187	2.242	69	0.602	3.883	146.6

TABLE IV. Lattice parameters of NPs obtained from SAED pattern and theoretical estimation.

	Lattice parameter	
Sample	a_{SAED}	$a_{\text{Theoretical}}$
Rh33Pd33Pt33	3.873	3.871
Rh50Pd25Pt25	3.853	3.854
Rh25Pd50Pt25	3.877	3.876
Rh25Pd25Pt50	3.882	3.883

Moreover, the shifting of peak position was observed in the profile for the NPs depending on the mixing ratio of Rh, Pd, and Pt ions in the solution. This feature strongly indicates that the fabricated particles possess the characteristics of solid-solution and composition controlled Rh–Pd–Pt alloy. The structural analysis followed by the XRD peak of (111) plane for the particles are summarized in Table III.

The crystalline size of NPs calculated from Scherrer's equation for full width at half maximum (FWHM) of (111) reflections showed larger values than that measured by TEM observation (Fig. 4), especially for Rh33Pd33Pt33 and Rh50Pd25Pt25 cases. This is probably due to the contribution of small number of large particles to the diffraction measurements. On the other hand, the crystalline size calculated by Scherrer's equation reflected the same as that of TEM observation in the case of Rh25Pd50Pt25 and Rh25Pd25Pt50. The lattice parameters obtained from (111) diffraction peaks were within the values of bulk Rh, Pd, and Pt and varied with the feeding ratios of the ions in

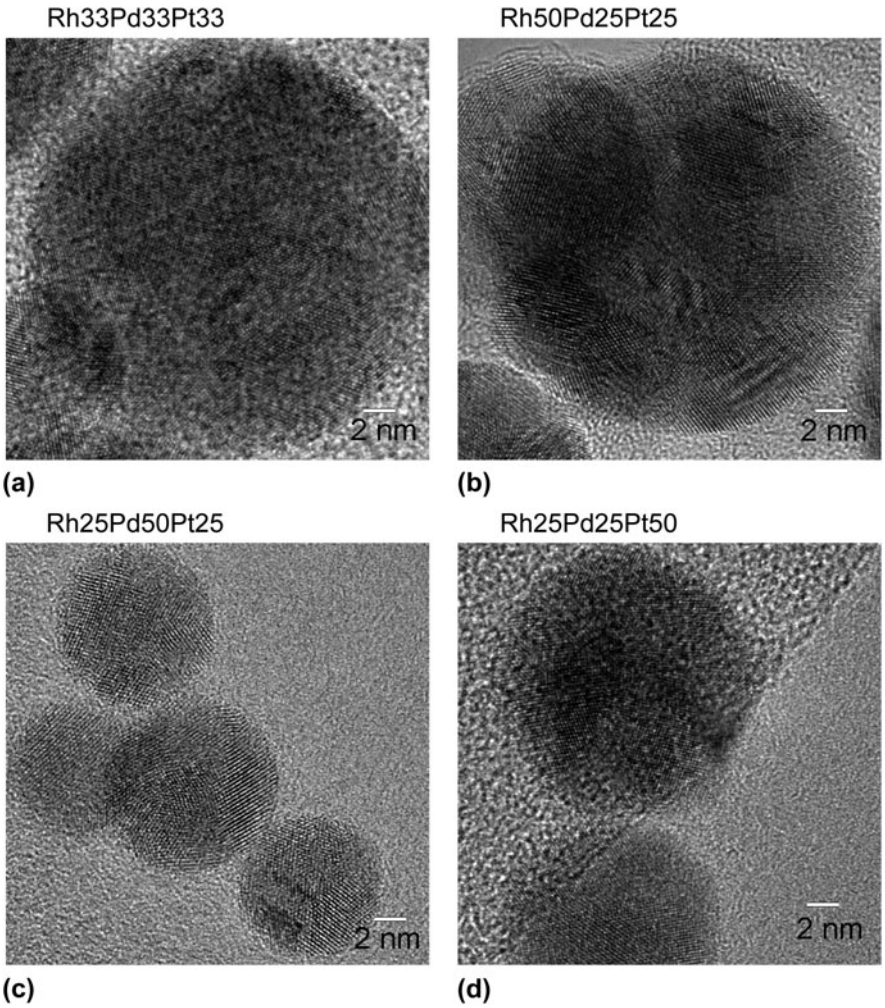


FIG. 6. HR-TEM images of NPs prepared in the solutions for different mixing ratios of ions (a) Rh33Pd33Pt33, (b) Rh50Pd25Pt25, (c) Rh25Pd50Pt25, and (d) Rh25Pd25Pt50.

https://doi.org/10.1557/jmr.2014.62 Published online by Cambridge University Press

the solutions. Using interplanar spacing of fcc structure, lattice parameter of NPs can be calculated as follows;

$$\frac{1}{d_{hkl}^2} = \frac{1}{a^2}\left(h^2 + k^2 + l^2\right), \quad (3)$$

where a is the lattice parameter and (hkl) is the given lattice plane. Experimental lattice parameters estimated using Eq. (3) as well as theoretical lattice parameters estimated by Vegard's law are shown in Table IV. Experimental lattice parameters are obtained from SAED patterns (Table IV) and from XRD peaks (Table III) showed a good agreement with the theoretical lattice parameters by Vegard's law. This agreement clearly demonstrates the fabrication of solid-solution Rh–Pd–Pt alloy NPs with intended compositions by femtosecond laser irradiation of a solution without any pre-added reducing agents.

The crystalline nature of the individual particles can also be confirmed through HR-TEM images (Fig. 6) of all the samples.

It is observed from HR-TEM images (Fig. 6) that each NP showed fringe patterns with segmented area. Therefore, the particles were polycrystalline.

The EDS analysis of selected particles, randomly chosen from sample solutions with different mixing ratios of ions, was performed to assess the composition of the individual particles (Fig. 7). It is noticeable from the EDS spectra that Rh, Pd, and Pt elements were detected in the particles. Table V shows the averaged composition of NPs obtained by EDS measurement for different sample solutions. Compositions of the particles were Rh37.4Pd32.4Pt30.2, Rh52.5Pd25.9Pt21.6, Rh28.5Pd42.3Pt29.2, and Rh23.3Pd25.5Pt51.1 formed in Rh33Pd33Pt33, Rh50Pd25Pt25, Rh25Pd50Pt25, and Rh25Pd50Pt25 sample solutions, respectively. The atomic compositions of Rh–Pd–Pt alloy NPs estimated from EDS were in good agreement with the initial feeding ratios of precursor sample solution. This indicates the complete reduction of metal ions forming homogeneous alloy NPs.

Jakobi et al. reported the stoichiometry of PtIr alloy NPs during laser ablation.[24] It is assumed that very similar properties of parent materials, i.e., heat of evaporation and density lead to simultaneous condensation of the ablated species, and thus the resulting particles preserve the target's stoichiometry. The heat of evaporation of Pt is 510 kJ mol^{-1} and Ir is 604 kJ mol^{-1} corresponding to a factor of 1.18 difference.

On the other hand, Kuhn et al.[25] reported the disproportionation of the resultant materials during laser ablation

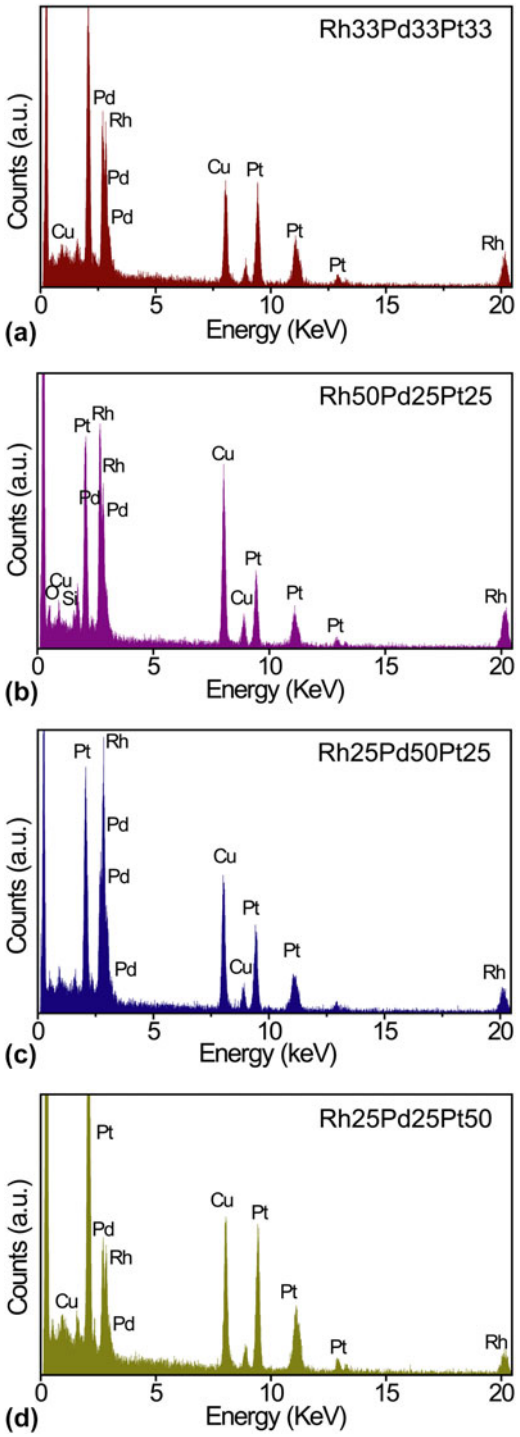


FIG. 7. EDS spectra of alloy NPs for (a) Rh33Pd33Pt33, (b) Rh50Pd25Pt25, (c) Rh25Pd50Pt25, and (d) Rh25Pd25Pt50.

TABLE V. Elemental composition of alloy NPs evaluated by EDS measurement.

	Compositions in the nanoparticles (at.%)		
Sample	Rh	Pd	Pt
Rh33Pd33Pt33	37.4	32.4	30.2
Rh50Pd25Pt25	52.5	25.9	21.6
Rh25Pd50Pt25	28.5	42.3	29.2
Rh25Pd25Pt50	23.3	25.5	51.2

https://doi.org/10.1557/jmr.2014.62 Published online by Cambridge University Press

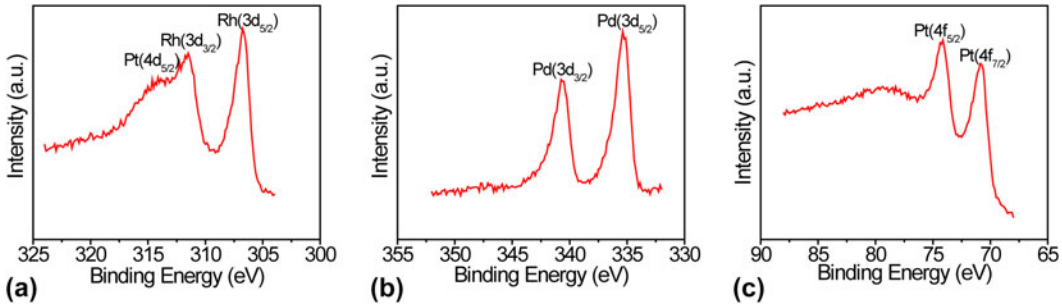


FIG. 8. XPS spectra of Rh33Pd33Pt33 alloy NPs for different binding energies: (a) Rh 3*d*, (b) Pd 3*d*, and (c) Pt 4*f*.

of brass because of the larger difference of heat of evaporation of Cu and Zn, 300 kJ mol^{-1} and 119 kJ mol^{-1}, respectively (a factor of 2.52 difference). Accordingly, in our case, the heat of evaporation of Rh is 494 kJ mol^{-1}, Pt is 510 kJ mol^{-1}, and for Pd is 372.4 kJ mol^{-1}, corresponding to factors of 1.03 and 1.32 differences, respectively. Therefore, materials stoichiometry was preserved in our study due to the simultaneous condensation.

XPS measurement was performed to determine the chemical state of Rh, Pd, and Pt elements in the alloy NPs. For XPS measurements, the NPs were supported on an indium foil to avoid peak overlapping. Figure 8 shows the XPS spectra of Rh33Pd33Pt33 NPs in the different energy regions corresponding to the Rh 3*d*, Pd 3*d*, and Pt 4*f* and 4*d* binding energies. According to XPS measurement, XPS peaks of Rh $3d_{5/2}$ and Rh $3d_{3/2}$ at 306.6 eV and 311.5 eV in Fig. 8(a) are assigned to the peaks of metallic state of Rh.[26] On the other hand, a shoulder observed at 314.1 eV is assigned to Pt $4d_{5/2}$ peak for metallic Pt.[26,27] In a similar fashion, XPS peaks exhibited at 335.3 eV and 340.75 eV in Fig. 8(b) are assigned to Pd $3d_{5/2}$ and Pd $3d_{3/2}$ peaks of metallic state of Pd.[26] Furthermore, the XPS peaks exhibited at 74.09 eV and 70.725 eV in Fig. 8(c) are assigned to Pt $4f_{7/2}$ and Pt $4f_{5/2}$ peaks of Pt metallic state.[26] These results demonstrate that alloy NPs were composed of metallic Rh, Pd, and Pt. Therefore, it can be concluded that, all the Rh, Pd, and Pt atoms in the alloy NPs are in the metallic state.

The formation of ternary Rh–Pd–Pt alloy NPs by the intense laser irradiation of mixed aqueous solution of Rh, Pd, and Pt ions can be attributed to optical decomposition of water molecules. The energetic radicals are generated due to avalanche ionization and/or multiphoton absorption of water molecules.[20] When solvated electrons or hydrogen radicals meet metal ions, the ions will be reduced to zero-valent atoms. As a result, alloy formation occurs due to coalescence and collision among the atoms in the solution during laser irradiation. When the particles become several nanometers in size, most of the atoms generated by laser irradiation are consumed and the growth of particles is terminated. As a result, composition controlled solid-solution alloy formation occurs, and this has been confirmed by EDS spectra and XRD measurements.

The elemental composition of NPs showed good agreement with the feeding ratios as confirmed by EDS measurement. XPS study revealed that three different elements involved in alloy NPs are in metallic state, indicating complete reduction of metal ions by laser irradiation. This is due to the strong reducing power of solvated electron and hydrogen radicals (−2.87 eV) produced in the aqueous solution by high intensity laser irradiation. Following this mechanism, we have successfully fabricated solid-solution Rh–Pd–Pt alloy NPs with controlled compositions. Catalytic measurement of this alloy NPs is our ongoing project and will be reported somewhere else.

IV. CONCLUSIONS

In this study, solid-solution Rh–Pd–Pt ternary alloy NPs have been successfully fabricated through femtosecond laser irradiation in a solution without any pre-added reducing agents. The formation of ternary alloy particles was confirmed by TEM observation, electron and XRD techniques. The existence of Rh, Pd, and Pt in the NPs was verified from the results of EDS and XPS. XPS study showed that the electronic states of the elements in alloy NPs were pure metallic. HR-TEM observation revealed that the NPs exhibited well-defined crystalline structure, regardless of the nanoparticle composition. It is also noticed that the alloy NPs prepared through femtosecond laser irradiation of a metallic ion solution are free from any pre-added reducing agents; therefore, the practical applications using these NPs are highly expected.

REFERENCES

1. S. Link, Z.L. Wang, and M.A. El-Sayed: Alloy formation of gold–silver nanoparticles and the dependence of the plasmon absorption on their composition. *J. Phys. Chem. B* **103**, 3529 (1999).
2. RF. Service: Small clusters hit the big time. *Science* **271**, 920 (1996).
3. Y. Zeng, Y. Wang, J. Jiang, and Z. Jin: Rh nanoparticle catalysed hydrogenation of olefins in the thermoregulated ionic liquid. *Catal. Commun.* **19**, 70 (2012).
4. J.R. Renzas, W. Huang, Y. Zhang, M.E. Grass, and G.A. Somorjai: $Rh_{1-x}Pd_x$ nanoparticle composition dependence in CO oxidation by NO. *Catal. Lett.* **141**, 235 (2011).

https://doi.org/10.1557/jmr.2014.62 Published online by Cambridge University Press

5. H. Zhang and N. Toshima: Preparation of novel Au-Pt-Ag trimetallic nanoparticles and their high catalytic activity for aerobic glucose oxidation. *Appl. Catal. A: General* **400**, 9 (2011).
6. M.A. Newton, B. Jyoti, A.J. Dent, S. Diaz-Moreno, S.G. Fiddy, and J. Evans: The impact of phase changes, alloying and segregation in supported RhPd catalysts during selective NO reduction by H_2. *Chem. Phys. Chem.* **5**, 1056 (2004).
7. J.R. Renzas, W. Huang, Y. Zhang, M.E. Grass, D.T. Hoang, S. Alayoglu, D.R. Butcher, F.F. Tao, Z. Liu, and G.A. Somoraji: Rh(1-x)Pd(x) nanoparticle composition dependence in CO oxidation by oxygen: Catalytic activity enhancement in bimetallic systems. *Phys. Chem. Chem. Phys.* **13**, 2556 (2010).
8. K. Siepen, H. Bönnemann, W. Brijoux, J. Rothe, and J. Hormes: EXAFS/XANES, chemisorption and IR investigation of colloidal Pt/Rh bimetallic catalysts. *Appl. Organomet. Chem.* **14**, 549 (2000).
9. C.E. Lyman, R.E. Lakis, and H.G. Stenger: X-ray emission spectrometry of phase separation in Pt-Rh nanoparticles for nitric oxide reduction. *Ultramicroscopy* **58**, 25 (1995).
10. X. Zhang, F. Zhang, and K.Y. Chan: Preparation of Pt–Ru–Co trimetallic nanoparticles and their electrocatalytic properties. *Catal. Commun.* **5**, 749 (2004).
11. L. Wang and Y. Yamauchi: Strategic synthesis of trimetallic Au@Pd@Pt core-shell nanoparticles from Poly(vinylpyrrolidone)-based aqueous solution toward highly active electrocatalysts. *Chem. Mater.* **23**, 2457 (2011).
12. H. Zhang and N. Toshima: Glucose oxidation using Au-containing bimetallic and trimetallic nanoparticles. *Catal. Sci. Technol.* **3**, 268 (2013).
13. T. Matsushita, Y. Shiraishi, S. Horiuchi, and N. Toshima: Synthesis and catalysis of polymer-protected Pd-Ag-Rh trimetallic nanoparticles with a core–shell structure. *Bull. Chem. Soc. Jpn.* **80**, 1217 (2007).
14. S.H. Tsai, Y.H. Liu, P.L. Wu, and C.H. Yeh: Preparation of Au–Ag–Pd trimetallic nanoparticles and their application as catalysts. *J. Mater. Chem.* **13**, 978 (2003).
15. G.C. Bond: The electronic structure of platinum-gold alloy particles. *Platinum. Met. Rev.* **51**, 63 (2007).
16. Y. Herbani, T. Nakamura, and S. Sato: Femtosecond laser-induced formation of gold rich nanoalloys from the aqueous mixture of gold-silver ions. *J. Nanomater.* **2010**, 154210 (2010).
17. T. Nakamura, Y. Herbani, and S. Sato: Fabrication of solid-solution gold-platinum nanoparticles with controllable compositions by high-intensity laser irradiation of solution. *J. Nanopart. Res.* **14**, 785 (2012).
18. M.S.I. Sarker, T. Nakamura, Y. Herbani, and S. Sato: Fabrication of Rh based solid solution bimetallic alloy nanoparticles with fully tunable composition through femtosecond laser irradiation in aqueous solution. *Appl. Phys. A* **110**, 145 (2013).
19. Y. Herbani, T. Nakamura, and S. Sato: Synthesis of platinum-based binary and ternary alloy nanoparticles in intense laser field. *J. Coll. Interface Sci.* **375**, 78 (2012).
20. S. Pommeret, F. Gobert, M. Mostafavi, I. Lampre, and J.C. Mialocq: Femtochemistry of hydrated electron at decimolar concentration. *J. Phys. Chem. A* **105**, 11400 (2001).
21. S.L. Chin and S. Legacé: Generation of H_2, O_2 and H_2O_2 from water by the use of intense femtosecond laser pulses and the possibility of laser sterilization. *Appl. Opt.* **35**, 907 (1996).
22. K. Yuge: Concentration effects on segregation behavior of Pt-Rh nanoparticles. *Phys Rev B* **84**, 085451 (2011).
23. L. Vegard and H. Dale: Untersuchungen ueber Mischkristalle und Legierungen. *J. Kristallogr.* **67**, 148 (1928).
24. J. Jakobi, A. Menendez-Manjon, V.S.K. Chakravadhanula, L. Kienle, P. Wagener, and S. Barcikowski: Stoichiometry of alloy nanoparticles from laser ablation of PtIr in acetone and their electrophoretic deposition on PtIr electrodes. *Nanotechnology* **22**, 145601 (2011).
25. H.R. Kuhn and D. Günter: Elemental fractionation studies in laser ablation inductively coupled plasma mass spectrometry on laser-induced brass aerosols. *Anal. Chem.* **75**, 747 (2003).
26. B.V. Christ: *Hand Book of Monochromatic XPS Spectra* (Wiley, New York, 2000).
27. J.Y. Park, Y. Zhang, M. Grass, T. Zhang, and G.A. Somoraji: Tuning of catalytic CO oxidation by changing composition of Rh-Pt bimetallic nanoparticles. *Nano. Lett.* **8**, 673 (2008).

https://doi.org/10.1557/jmr.2014.62 Published online by Cambridge University Press